JOURNAL OF COMPUTATIONAL PHYSICS **137,** 101–129 (1997)
ARTICLE NO. CP975796

# Numerical Method for Incompressible Vortical Flows with Two Unbounded Directions

Steven C. Rennich and Sanjiva K. Lele[1]

*Department of Aeronautics and Astronautics, Stanford University, Stanford, California 94305-4035*
E-mail: lele@leland.stanford.edu

Received October 30, 1996; revised May 19, 1997

A new, efficient, and accurate method has been developed for computing unsteady, incompressible, viscous flows in a domain where two dimensions are unbounded, the third dimension is periodic and the vorticity is rapidly decaying in the unbounded directions. We use the term unbounded to mean doubly infinite (no boundaries of any kind). This is an extension of the methods described by others for flows with two periodic and one unbounded direction, where the irrotational velocities outside the vortical domain are treated analytically. The new method is shown to be both accurate and efficient. The method presented here has finite, but arbitrarily high order, formal accuracy, and incurs substantial additional cost for a given mesh. However, this increased cost is more than offset by the reduction in the number of mesh points required for a given accuracy. The result is that for accurate computations, the present method can be orders of magnitude more efficient than others currently in use. This paper presents the method, discusses implementation issues, validates its accuracy, and presents sample calculations. 

## 1. INTRODUCTION

Many current scientific studies involve incompressible, vortical flows that reside in domains which are unbounded in two directions and periodic in the third. An example is the problem that motivated our study, the temporal evolution of aircraft wake vortices. Other problems of this type include the growth, stability, and mixing

[1] Also affiliated with the Stanford University Department of Mechanical Engineering.



0021-9991/97 $25.00

behavior of 3D jets and wakes. Due to their unbounded nature, the accurate simulation of these flows can be expensive.

Many efficient and accurate methods have been developed for domains which are unbounded in only one direction. These methods [1–5] involve mapping the infinite physical domain to a finite computational domain and applying finite difference, Chebyshev or Fourier spectral methods on the mapped domain. Canuto *et al.* [6] discusses many of these methods, which have been used extensively. When these methods are applied to problems which are infinite in two directions, a large portion of the mesh points, which are required by the mapping, lie outside the domain of interest. Their efficiency suffers accordingly.

Recently, methods have been developed for 1D unbounded flows which, assuming incompressibility and compact vorticity, represent the far-field velocities with analytic functions [7–9]. The method due to Corral and Jiménez [8] is particularly attractive. It retains the resolution and efficiency characteristics of Fourier spectral methods and enforces the infinite boundary conditions exactly with negligible cost. This method has been used and extended to allow for mean growth by Sondergaard [10]. Unfortunately, these 1D unbounded methods can only be applied to problems with two unbounded directions by extending a second dimension to a suitable distance and applying a periodic boundary condition. This severely limits the accuracy and adds a large computational overhead.

The success of the method due to Corral and Jiménez in 1D unbounded flows motivated us to extend it to flows which are unbounded in two directions. This extension is presented in Section 2. Pertinent aspects of our implementation are presented in Section 3. The accuracy and convergence characteristics of this new method are presented in Section 4, 5, and 6. Section 7 compares its performance to other applicable methods in terms of efficiency. Section 8 presents the results of two sample computations.

## 2. THEORY

### 2.1. *Analytical Matching in One Dimension*

The method we present uses an analytical representation for the velocity outside of the computational domain. This idea is not new and has been applied to vortical flows which have one unbounded direction and have rapidly decaying vorticity in that direction. Spalart [9] efficiently and accurately represented such flows using Jacobi polynomials as basis functions. Rapid convergence of the velocity was achieved by recognizing that the irrotational velocity, outside the domain of interest, obeys Laplace's equation and must decay as $O(e^{-\gamma|x|})$. Here $\gamma$ is the magnitude of the wave-vector in the periodic directions and $x$ is the coordinate in the unbounded direction. For wave-vectors of small magnitude, the decay is slow and the domain must be extended to large distances before an ''infinite'' boundary condition can be applied. However, if ''extra'' basis functions, which decay like $e^{-\gamma|x|}$, are included for every wave-vector, the infinitely distant boundaries can be represented exactly.

Corral and Jiménez [8] extended this idea by noting that these slowly decaying velocity modes need not be included in the set of basis functions at all. The amplitude

of these modes can be computed from the amplitudes of the other, rapidly decaying modes. In this way the irrotational modes can be used as a boundary condition, or correction, to the solution obtained using only the rapidly decaying modes. Using this approach, they developed a scheme which used Fourier spectral methods in a domain with finite extent and periodic boundary conditions. The unbounded character was achieved by adding an irrotational correction to the velocity. Again, this requires that the vorticity in the problem decay rapidly in the unbounded direction. This irrotational correction requires negligible computational effort. Corral and Jiménez also describe a technique for treating the viscous terms implicitly, which is fully compatible with the method presented in this paper.

### 2.2. *Analytical Matching in Two Dimensions*

The efficiency and accuracy characteristics of Fourier spectral methods are well known and the negligible cost of the extension to infinity make the Corral and Jiménez scheme very attractive. Here we extend this scheme to domains which are unbounded in two dimensions and periodic in the third. Note that the use of spectral methods is not required for the implementation of the infinitely distant boundaries. Anderson and Reider [11] have used similar ideas in the formulation of a finite-difference method for the 2D flow about a circular cylinder in an unbounded domain. Our derivation does not assume a familiarity with the previous work and we approach the problem in a substantially different manner.

Before presenting the method, we should define exactly the class of flows we intend to solve. The flows we are interested in are unsteady, incompressible, viscous flows in a domain where two directions are unbounded and the other is periodic. For the derivation of this method, we will make the further assumption that the vorticity is compactly distributed in the unbounded directions, such that the vorticity decays to zero in some finite distance. Because this last assumption will, in practice, rarely be met, the performance of this method when vorticity exists on the matching boundary is discussed in Section 5.

The governing equation for incompressible, unsteady flow can be written in vorticity form as

$$\frac{\partial \boldsymbol{\omega}}{\partial t} = -\nabla \times (\boldsymbol{\omega} \times \mathbf{u}) + \frac{1}{\mathrm{Re}} \nabla^2 \boldsymbol{\omega} \tag{1}$$

where $\mathbf{u}$ is the velocity field, $\boldsymbol{\omega}$ is the vorticity field, $t$ is time, and Re is a Reynolds number which is assumed to be constant. This equation has been nondimensionalized with appropriately chosen length and velocity scales. Given an initial condition on vorticity, the difficulty in solving (1) lies in determining $\mathbf{u}$ efficiently. Once $\mathbf{u}$ is known, a variety of efficient methods exist for advancing the equation in time.

In developing the method, reference will be made to the domain decomposition and coordinate systems defined in Fig. 1. The domain is decomposed into three regions. The first region, termed the internal domain, is the space occupied by a circular cylinder just large enough to contain *all* of the vorticity in the problem. The cylindrical surface of this domain is termed the matching boundary. The second

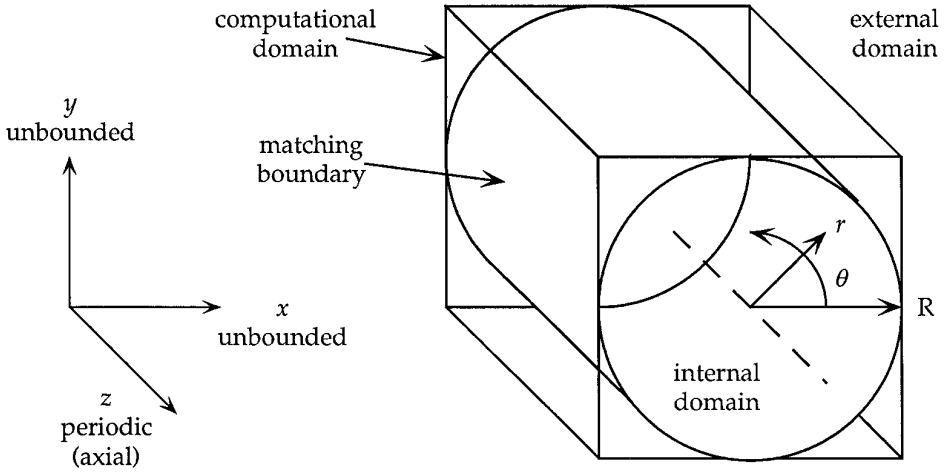


**FIG. 1.** Diagram showing the coordinate systems and domains used in this work.

region, termed the external domain, is infinitely large and represents all space not in the internal domain. The third region, which we call the computational domain, is the space occupied by a square cylinder just large enough to contain the internal domain. Thus the internal and external domains are mutually exclusive and the computational domain contains the entire internal domain and part of the external domain.

Both cartesian $(x, y, z)$ and cylindrical polar $(r, \theta, z)$ coordinate systems will be used in developing the method. In cartesian coordinates the velocity has components $\mathbf{u} = (u_x, u_y, u_z)$ with $u_z$ being the component in the axial (periodic) direction. In cylindrical polar coordinates the velocity has components $\mathbf{u} = (u_r, u_\theta, u_z)$, where $u_z$ is unchanged. The polar coordinate system will always be centered in the cartesian system such that the matching surface is a surface of constant radius, $R$. The polar coordinate system must extend to a distance of at least $r = \sqrt{2}\ R$ in order to discretize that portion of the computational space which lies in the external domain. The symbols $\mathbf{e}_r$, $\mathbf{e}_\theta$, and $\mathbf{e}_z$ will be used to represent the unit vectors in cylindrical polar coordinates.

2.2.1. *Velocity decomposition.* The efficient computation of the velocity field begins by decomposing $\mathbf{u}$ into a vortical part, $\mathbf{u}_V$, a potential part, $\nabla\phi$, and a uniform flow part to accommodate the free-stream condition, $\mathbf{u}_\infty$:

$$\mathbf{u} = \mathbf{u}_V + \nabla\phi + \mathbf{u}_\infty. \tag{2}$$

Here $\mathbf{u}_V$ and $\phi$ are field quantities, and $\mathbf{u}_\infty$ is a constant. All of these variables are found from the given vorticity field except $\mathbf{u}_\infty$ which must be prescribed. Note that the classical decomposition of a velocity field into a solenoidal vector component, $\mathbf{u}_V$, and an irrotational scalar component, $\nabla\phi + \mathbf{u}_\infty$ is still present.

2.2.2. *Vortical velocity component.* The vortical velocity component, $\mathbf{u}_V$, is computed from the vorticity–velocity relation assuming periodicity in all three direc-

tions. This is easily done using Fourier spectral methods. However, since the Fourier inversion of the Laplacian cannot represent the zero wave-vector coefficients, the velocity due to the mean vorticity requires special treatment. Thus we define the vortical velocity component as

$$\mathbf{u}_V = \begin{cases} \mathbf{u}_v + (\Gamma r/2\pi R^2)\mathbf{e}_\theta + A\,\mathbf{e}_z & \text{for } r < R \text{ (internal domain)} \\ (\Gamma/2\pi r)\mathbf{e}_\theta + A\,\mathbf{e}_z & \text{for } r > R \text{ (external domain),} \end{cases} \tag{3}$$

where

$$\mathbf{u}_v = \nabla^{-2}(-\nabla \times \boldsymbol{\omega}) \tag{4}$$

is the Fourier spectral solution to the vorticity–velocity relation, $\Gamma$ is the mean axial circulation, and $A$ is a coefficient adjusted so that the mean axial velocity, outside the region of vorticity, is zero. This definition of $A$ ensures that the axial velocity is zero at $r = \infty$. (For example, jet flows require nonzero values for $A$.)

These definitions of $\Gamma$ and $A$ constitute an exact treatment of the velocity due to the mean axial and azimuthal vorticity, respectively, as they exist in a domain which is unbounded in two directions. Since, by assumption, the vorticity is compact and exists in a domain which is unbounded in $r$, there can be no mean radial vorticity. Both $\Gamma$ and $A$ are constant in time and need only be determined once from the initial conditions.

With this definition, $\mathbf{u}_V$ is made up of both rotational and irrotational velocities and contains the effects of infinitely many images of the (nonzero wave-vector) vorticity field.

2.2.3. *Potential velocity component.* The potential velocity, $\nabla\phi$, is a correction to the velocity field which removes the effects of all the image vorticity. The form of $\phi$ is determined analytically. Irrotational flow must satisfy, via continuity, Laplace's equation,

$$\nabla^2\phi = 0. \tag{5}$$

Cast in cylindrical polar coordinates, (5) becomes

$$\frac{1}{r}\frac{\partial}{\partial r}\left(r\frac{\partial\phi}{\partial r}\right) + \frac{1}{r^2}\frac{\partial^2\phi}{\partial\theta^2} + \frac{\partial^2\phi}{\partial z^2} = 0. \tag{6}$$

Taking the Fourier expansion of $\phi$ in the azimuthal and axial directions, defined as

$$\phi = \sum_m \sum_k \hat{\phi}_{mk}(r)e^{i(m\theta+kz)} \tag{7}$$

and substituting into (6) results in

$$r^2\frac{\partial^2}{\partial r^2}(\hat{\phi}_{mk}) + r\frac{\partial}{\partial r}(\hat{\phi}_{mk}) - (k^2r^2 + m^2)\hat{\phi}_{mk} = 0 \tag{8}$$

for each azimuthal wavenumber, $m$, and axial wavenumber, $k$. The hat symbol is used to denote the Fourier coefficient of a variable.

For all $k \neq 0$, Eq. (8) is Bessel's modified differential equation and thus the solutions are the modified Bessel functions of the first and second kinds. Since the velocity must be finite everywhere, solutions involving the modified Bessel function of the first kind, $\mathrm{I}_m$, apply to the internal domain while solutions involving the modified Bessel function of the second kind, $\mathrm{K}_m$, apply to the external domain:

$$\hat{\phi}_{mk} = \begin{cases} \mathrm{I}_m(|k|r) & \text{for } r < R \\ \mathrm{K}_m(|k|r) & \text{for } r > R \end{cases} \qquad (|k| \neq 0). \tag{9}$$

When $k = 0$, Eq. (8) becomes an Euler–Cauchy equation with solutions of the form $r^{|m|}$ and $r^{-|m|}$. Again, since the velocity must be finite everywhere, the $r^{|m|}$ solutions apply to the internal domain and the $r^{-|m|}$ solutions apply to the external domain.

$$\hat{\phi}_{m0} = \begin{cases} r^{|m|} & \text{for } r < R \\ r^{-|m|} & \text{for } r > R \end{cases} \qquad (|k| = 0). \tag{10}$$

The velocity potential can now be expressed as

$$\phi = \begin{cases} \displaystyle\sum_m \sum_{\substack{k \\ k\neq 0}} C_{mk}\mathrm{I}_m(|k|r)e^{i(m\theta+kz)} + \sum_m C_{m0}r^{|m|}e^{im\theta} & \text{for } r < R \\ \displaystyle\sum_m \sum_{\substack{k \\ k\neq 0}} D_{mk}\mathrm{K}_m(|k|r)e^{i(m\theta+kz)} + \sum_m D_{m0}r^{-|m|}e^{im\theta} & \text{for } r > R \end{cases} \tag{11}$$

and the velocity field can be expressed as

$$\mathbf{u} = \begin{cases} \mathbf{u}_v + \nabla\phi + (\Gamma r/2\pi R^2)\mathbf{e}_\theta + A\,\mathbf{e}_z + \mathbf{u}_\infty & \text{for } r < R \\ \nabla\phi + (\Gamma/2\pi r)\mathbf{e}_\theta + A\,\mathbf{e}_z + \mathbf{u}_\infty & \text{for } r > R. \end{cases} \tag{12}$$

2.2.4. *Velocity matching.* Equations (11) and (12) contain two unknown coefficients, $C_{mk}$ and $D_{mk}$, for every $(m, k)$ wavenumber pair. These coefficients are determined by matching two components of the internal velocity with two components of the external velocity on the matching surface. Despite the availability of only two matching parameters, all velocities and velocity derivatives can be matched. The radial and azimuthal velocity components will be matched first. This choice will then be shown to be equivalent to the matching of any other pair of velocities.

The conditions for matching radial and azimuthal velocities are

$$[(\mathbf{u}_v + \nabla\phi)\cdot\mathbf{e}_r]_{r=R^-} = [\nabla\phi\cdot\mathbf{e}_r]_{r=R^+} \tag{13}$$

and

$$[(\mathbf{u}_v + \nabla\phi)\cdot\mathbf{e}_\theta]_{r=R-} = [\nabla\phi\cdot\mathbf{e}_\theta]_{r=R+}, \tag{14}$$

where the subscripts, $r = R-$ or $r = R+$, denote that these terms are to be evaluated on the matching boundary using the form of the potential function which applies to the internal or external domain, respectively. Substituting (11) into (13) and (14), replacing the vortical velocity terms with their Fourier expansions, and invoking orthogonality gives, for Fourier components with $k \neq 0$,

$$|k|D_{mk}\mathrm{K}'_m(|k|R) - |k|C_{mk}\mathrm{I}'_m(|k|R) = \widehat{(\mathbf{u}_v\cdot\mathbf{e}_r)}_{\mathrm{mk}} \tag{15}$$

and

$$\frac{im}{R}D_{mk}\mathrm{K}_m(|k|R) - \frac{im}{R}C_{mk}\mathrm{I}_m(|k|R) = \widehat{(\mathbf{u}_v\cdot\mathbf{e}_\theta)}_{mk}, \tag{16}$$

where the primes denote derivatives of the Bessel functions with respect to their argument. For Fourier components with $k = 0$, the matching equations are

$$-|m|D_{m0}R^{-|m|-1} - |m|C_{m0}R^{|m|-1} = \widehat{(\mathbf{u}_v\cdot\mathbf{e}_r)}_{m0} \tag{17}$$

and

$$imD_{m0}R^{-|m|-1} - imC_{m0}R^{|m|-1} = \widehat{(\mathbf{u}_v\cdot\mathbf{e}_\theta)}_{m0}. \tag{18}$$

If instead, the radial and axial velocity components were used in the matching, (16) would, for $k \neq 0$, be replaced with

$$ikD_{mk}\mathrm{K}_m(|k|R) - ikC_{mk}\mathrm{I}_m(|k|R) = \widehat{(\mathbf{u}_v\cdot\mathbf{e}_z)}_{\mathrm{mk}}. \tag{19}$$

Multiplying (16) by $R/(im)$ and (19) by $ik$, equating right-hand sides, and rearranging gives

$$\frac{im}{R}\ \widehat{(\mathbf{u}_v\cdot\mathbf{e}_z)}_{mk} - ik\widehat{(\mathbf{u}_v\cdot\mathbf{e}_\theta)}_{mk} = 0. \tag{20}$$

This merely restates that the radial component of vorticity must be zero on the matching boundary. Since this is true by assumption, matching radial and azimuthal velocity is entirely equivalent to matching radial and axial velocity for $k \neq 0$. Thus, Eqs. (15)–(18) match all three components of velocity on the matching surface. The axial velocity cannot be used to match coefficients when $k = 0$ because no relation equivalent to (18) involving axial velocity can be formed. Likewise, the azimuthal velocity cannot be used to match coefficients when $m = 0$ and (19) must be used.

Since all components of velocity are continuous across the matching surface, which is a cylinder, all derivatives with respect to $\theta$ and $z$ must match. Continuity can then be used to show that all higher derivatives of velocity are continuous as

well. Thus, for smooth, compact vorticity distributions, the matching equations, (15)–(19), ensure that all velocities and all derivatives of velocity are continuous across the matching boundary.

Solving the matching equations gives

$$C_{mk} = \begin{cases} \dfrac{imK_m(\widehat{\mathbf{u}_v \cdot \mathbf{e}_r})_{mk} - R|k|\mathrm{K}'_m(\widehat{\mathbf{u}_v \cdot \mathbf{e}_\theta})_{mk}}{im|k|(\mathrm{I}_m\mathrm{K}'_m - \mathrm{I}'_m\mathrm{K}_m)} & \text{for } (k, m \neq 0) \\ -\dfrac{(\widehat{\mathbf{u}_v \cdot \mathbf{e}_r})_{m0}}{2|m|R^{|m|-1}} - \dfrac{(\widehat{\mathbf{u}_v \cdot \mathbf{e}_\theta})_{m0}}{2imR^{|m|-1}} & \text{for } (k = 0) \\ \dfrac{k\mathrm{K}_0(\widehat{\mathbf{u}_v \cdot \mathbf{e}_r})_{0k} + i|k|\mathrm{K}'_0(\widehat{\mathbf{u}_v \cdot \mathbf{e}_z})_{0k}}{k|k|(\mathrm{I}_0\mathrm{K}'_0 - \mathrm{I}'_0\mathrm{K}_0)} & \text{for } (m = 0), \end{cases} \tag{21}$$

where it is understood that all Bessel functions are evaluated at $|k|R$. Since the mean velocity terms have been treated exactly, $C_{00} = 0$. With $C_{mk}$ known, $D_{mk}$ is found from (15)–(19).

## 3. IMPLEMENTATION

Although the analysis in the previous section completely defines the computation of the velocity and thus the method, its success depends on efficient implementation. We have chosen Fourier spectral methods for the solution of (4). The standard fourth-order Runge–Kutta time advancement is used for (1). In the interest of efficiency, all of the required Bessel functions are computed once, taking advantage of the recursion relations [12], and stored.

De-aliasing of the nonlinear term in (1) is done by using the 2/3 rule on $\mathbf{u}_v$ and $\boldsymbol{\omega}$. The series representation of the potential velocity is not similarly truncated, but, since it is a linear function of the vorticity field, the coefficients for the upper 1/3 wavenumbers are zero.

Computation of the potential velocity field requires two interpolations. The vortical velocity, $\mathbf{u}_v$, constructed on a cartesian mesh, needs to be interpolated to points on the cylindrical matching boundary. The transform of these interpolated velocities are used in (21). Since the axial transform of the potential velocity is most easily formed on the cylindrical polar mesh, using (11), it needs to be interpolated back to the cartesian computational mesh to form the time derivative terms.

Both of these interpolations are performed using Lagrange interpolation of arbitrary order. By that we mean a fixed interpolation order is specified at startup and all interpolation weights are computed once and stored. In this way the interpolation fixes the formal accuracy of the method, but since it can be set arbitrarily high, it need not compromise the accuracy of the spectral computation of (4).

## 4. VALIDATION

Before this method can be confidently used, its accuracy and convergence characteristics must be confirmed. All aspects of our code have been independently

validated. However, since the new aspect of this method is the computation of velocity in a domain that is unbounded in two directions from a given vorticity field, only the validation of this step is presented. Before validation can begin, analytical representations of the vorticity distribution and the associated velocity distribution are required for comparison. These analytical functions are developed first.

### 4.1. *Test Cases*

The test cases for the velocity computation were constructed by solving the 3D linearized perturbation equations for an inviscid, incompressible, axisymmetric columnar vortex with potentially nonzero axial velocity. The derivation of these equations and the computation of their associated eigenfunctions has been performed by many others. The equations will be briefly outlined here. We refer the reader to other works for details [13–15].

We begin with the 3D incompressible Euler equations,

$$\begin{aligned} \nabla \cdot \mathbf{u} &= 0 \\ \frac{D\mathbf{u}}{Dt} &= -\frac{\nabla p}{\rho_0}, \end{aligned} \tag{22}$$

where $\mathbf{u}$ is the velocity vector, $p$ is the pressure, and $\rho_0$ is the (constant) density. A standard linear stability analysis of (22), assuming perturbation quantities of the form

$$q = \sum_m \sum_k \hat{q}_{mk}(r) e^{\sigma t} e^{i(m\theta + kz)}, \tag{23}$$

where $q$ represents any perturbation quantity, results in four equations for the perturbation velocities and pressure. The boundary conditions are formed from the requirements that the perturbation be smooth at $r = 0$ and that all perturbations decay to zero at $r = \infty$. Solving the coupled system for one of the velocities gives the dispersion relation (eigenvalues) and eigenfunctions of the different perturbation modes (see [13, Eq. (18)]).

The mean velocity profiles used when computing the perturbation eigenfunctions are very important. To work well with the Fourier spectral methods, the associated mean vorticity must be smooth. To satisfy the assumptions of the method given in this paper, the mean vorticity must be compact, but, to assess the benefit of the boundary conditions, the velocity must *not* be compact. A mean vorticity/velocity profile satisfying these requirements has been constructed. These profiles have been nondimensionalized using $r_0$, $\Gamma_0/r_0$, and $\Gamma_0/r_0^2$ as reference length, velocity, and vorticity scales, respectively. The mean vortex radius, $r_0$, is defined as the location of maximum azimuthal velocity and $\Gamma_0$ is the circulation of the mean vortex. We

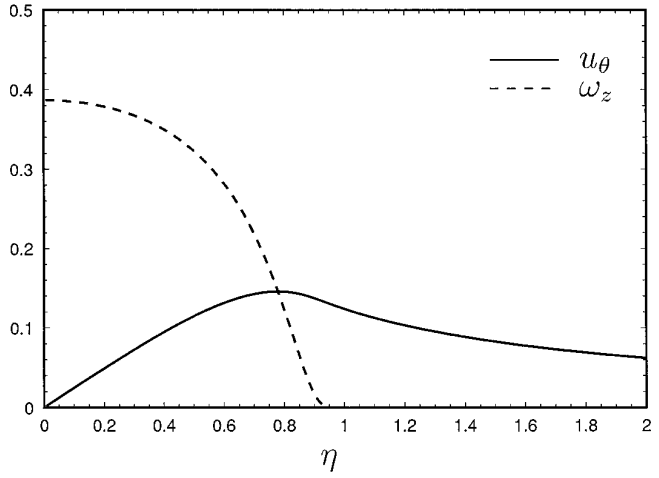


**FIG. 2.** The mean azimuthal velocity and axial vorticity distributions.

define a scaling $\eta = cr$ and use the following distribution for mean axial velocity which contains both a rotational and an irrotational component:

$$u_\theta = \frac{c}{2\pi}\begin{cases} \frac{1}{\eta} + \left(\eta - \frac{1}{\eta}\right)\exp\left(\frac{\eta^2}{\eta^2-1}\right) & \text{for } \eta \le 1 \\ \frac{1}{\eta} & \text{for } \eta \ge 1. \end{cases} \tag{24}$$

The coefficient $c = 0.7795028144572484$ is set to correctly scale the vortex. The associated vorticity distribution is

$$\omega_z = \frac{c^2}{\pi}\begin{cases} \frac{\eta^2-2}{\eta^2-1}\exp\left(\frac{\eta^2}{\eta^2-1}\right) & \text{for } \eta \le 1 \\ 0 & \text{for } \eta \ge 1. \end{cases} \tag{25}$$

The advantage these distributions have over those used by others [16] is that explicit formulas exist for both the mean vorticity and the mean velocity which simplifies the computation of errors. Figure 2 shows these mean profiles. The compact character of the vorticity and the noncompact character of the velocity is apparent.

Vortices with an axial velocity component in the mean flow are also considered. For convenience, the same distribution as in (25) (vorticity) is used, scaled by the parameter $V_z$:

$$u_z = V_z\begin{cases} \frac{\eta^2-2}{\eta^2-1}\exp\left(\frac{\eta^2}{\eta^2-1}\right) & \text{for } \eta \le 1 \\ 0 & \text{for } \eta \ge 1. \end{cases} \tag{26}$$

To test all aspects of the code, four test cases will be considered.

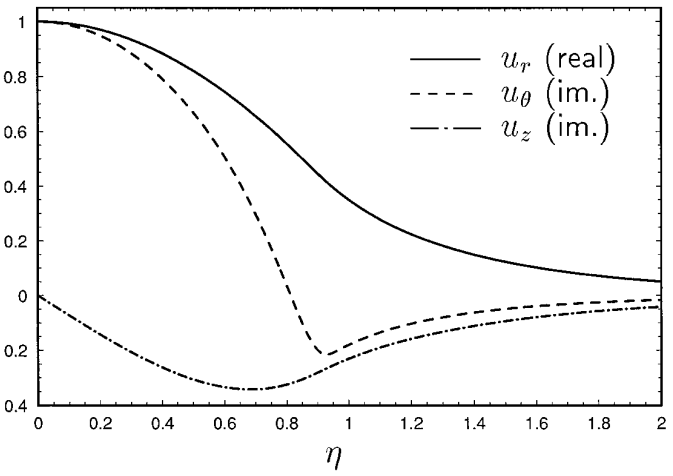


**FIG. 3.** Radial profiles of the axial and azimuthal Fourier transforms of the perturbation velocity for Case 2. All components not shown are zero.

4.1.1. *Case* 1. Case 1 tests the convergence of velocity induced by an axisymmetric columnar vortex with no axial flow ($V_z = 0$). The mean ($m, k = 0$) axial vorticity mode is the mode for which velocity decays most slowly with radius, extending well beyond the vortical region. This is often the mean flow in cases of interest. This case verifies the matching conditions for the $k = 0$ wavenumber components. The vorticity and velocity profiles are as shown in Fig. 2, but scaled such that the maximum velocity magnitude is unity.

4.1.2. *Case* 2. Case 2 tests the convergence of velocity due to the first azimuthal mode vorticity perturbation of the mean vortex without any axial flow ($m, k = 1$, $V_z = 0$). This verifies the matching conditions for general axial and azimuthal wavenumber. The eigenvalue, from (23), for this perturbation is $\sigma = (0.0, 0.0528623)$. For this case the mean vorticity is omitted and the perturbation velocities are scaled such that the maximum velocity magnitude is unity. The perturbation velocity profiles for this case are shown in Fig. 3. The perturbation vorticity profiles are shown in Fig. 4.

4.1.3. *Case* 3. Case 3 tests the convergence of velocity due to an axisymmetric vorticity perturbation of the mean vortex with axial flow ($k = 2$, $m = 0$, and $V_{z0} = 1/2$). This case verifies the matching conditions for $m = 0$. The eigenvalue for this case is $(0.0, 0.0752124)$. Again, the mean flow is omitted and the perturbation velocities are scaled such that the maximum velocity magnitude is unity. The perturbation velocity profiles for this case are shown in Fig. 5. The perturbation vorticity profiles are shown in Fig. 6.

4.1.4. *Case* 4. Case 4 tests the convergence of velocity due to a fairly arbitrary perturbation to the mean vortex. This perturbation is of higher order in the azimuthal direction, has strong axial flow, has strong gradients in the perturbation quantities, and is included to show trends in the convergence characteristics. For

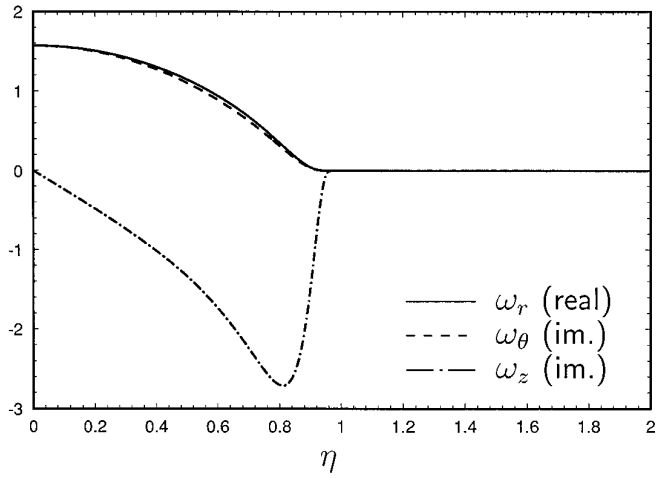


**FIG. 4.** Radial profiles of the axial and azimuthal Fourier transforms of the perturbation vorticity for Case 2. All components not shown are zero.

this case, $k = 1.5$, $m = 2$, and $V_z = 15$. The high axial velocity is required to prevent extremely sharp gradients. The eigenvalue for this case is $(-0.443334, -1.41786)$. Again, the mean flow is omitted and the perturbation velocities are scaled such that the maximum velocity magnitude is unity. The perturbation velocity profiles are shown in Fig. 7. The perturbation vorticity profiles are shown in Fig. 8.

### 4.2. *Velocity Convergence*

To test the effectiveness of the analytical matching boundary treatment, the global error in velocity versus the number of azimuthal wavenumbers retained in

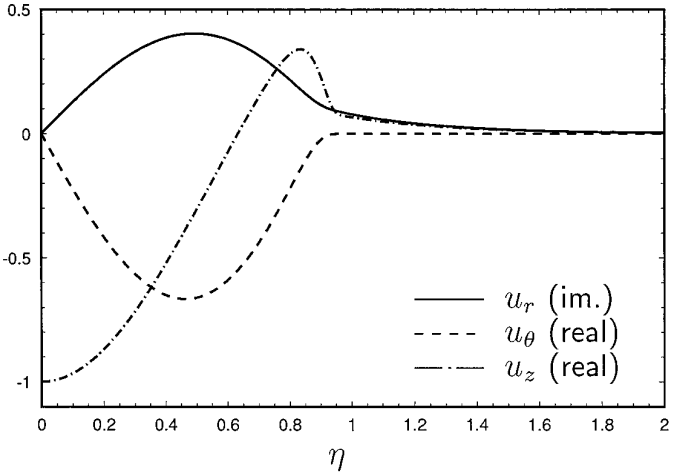


**FIG. 5.** Radial profiles of the axial and azimuthal Fourier transforms of the perturbation velocity for Case 3. All components not shown are zero.

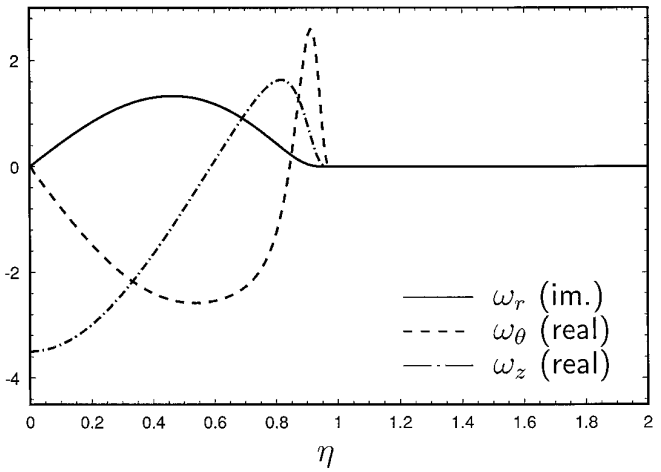


**FIG. 6.** Radial profiles of the axial and azimuthal Fourier transforms of the perturbation vorticity for Case 3. All components not shown are zero.

the analytical matching, $N_\theta$, is computed for each test case. These tests are designed, as much as possible, to isolate this effect. They are run in a domain whose $x$ and $y$ dimensions are exactly equal to the cross-axial extent of vorticity ($\eta = 1$), thus ensuring that there is zero vorticity on the matching boundary. A $256 \times 256 \times 4$ cartesian mesh and a 192 (radial) by 512 (azimuthal) polar mesh is used. Since each test case contains only one axial wavenumber, the low axial resolution is sufficient. The dense cross-axial cartesian mesh permits very accurate computation of the vorticity–velocity relation (4). The dense polar mesh, kept constant regardless of the number of matching modes actually used, and ninth-order accurate Lagrange

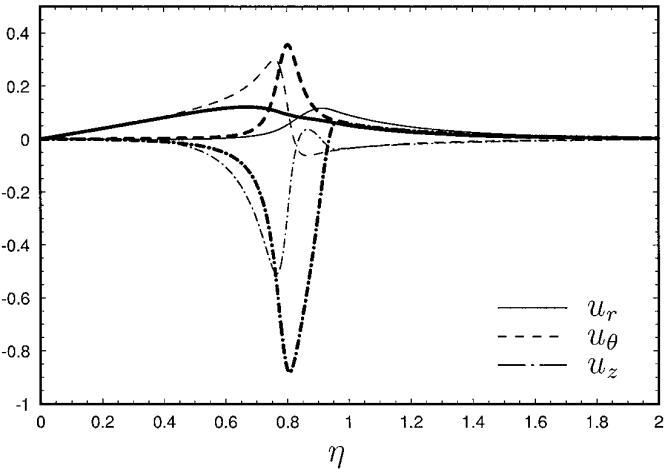


**FIG. 7.** Radial profiles of the axial and azimuthal Fourier transforms of the perturbation velocity for Case 4. Thick lines correspond to the real components and thin lines correspond to the imaginary components.

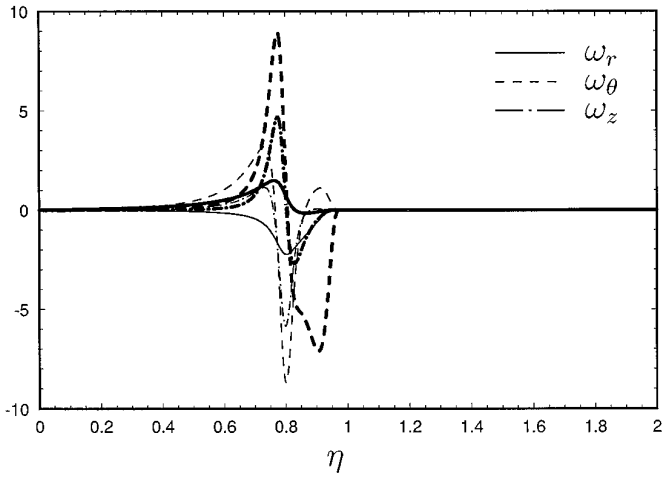


**FIG. 8.** Radial profiles of the axial and azimuthal Fourier transforms of the perturbation vorticity for Case 4. Thick lines correspond to the real components and thin lines correspond to the imaginary components.

interpolation allow very accurate polar-cartesian interpolation. All vorticity fields are scaled so that the peak velocities are unity, permitting direct comparison of the errors. In all cases the global velocity error is computed as

$$\|\mathbf{u} - \mathbf{u}^*\| = \left[\frac{1}{V}\int_V |\mathbf{u} - \mathbf{u}^*|^2 \, dV\right]^{1/2}, \tag{27}$$

where $\mathbf{u}^*$ represents the exact (reference) velocity field and $\mathbf{u}$ is the computational result. $V$ is the volume of the computational domain which means that the error norm contains contributions from both the internal and external domains.

The results of this test, shown in Fig. 9, demonstrate that in all cases the error in velocity converges spectrally with $N_\theta$ until saturation. The matching conditions do indeed work very well. This test also demonstrates that the domain need only contain the vortical fluid—no extra space is needed between the vortical region and the boundaries of the computational domain.

To examine the convergence of the scheme as a whole, Figs. 10 and 11 plot the velocity error versus the cross-axial mesh resolution, $N_x$, $N_y$, for Cases 1 and 4, respectively. In both cases the axial resolution is kept constant at 4 and the parameters $N_x$, $N_y$, and $N_\theta$ are varied together. The order of accuracy of the interpolation scheme is also varied in each case to illustrate its importance. Both cases show that the global velocity error decreases with increasing mesh resolution. Figure 10 shows that the order of accuracy of the method is formally limited by the order of the interpolation scheme used. Figure 11 indicates that, for more complex flows, it is not necessary to use unusually high order interpolation to preserve the advantages of the Fourier spectral solution of (4).

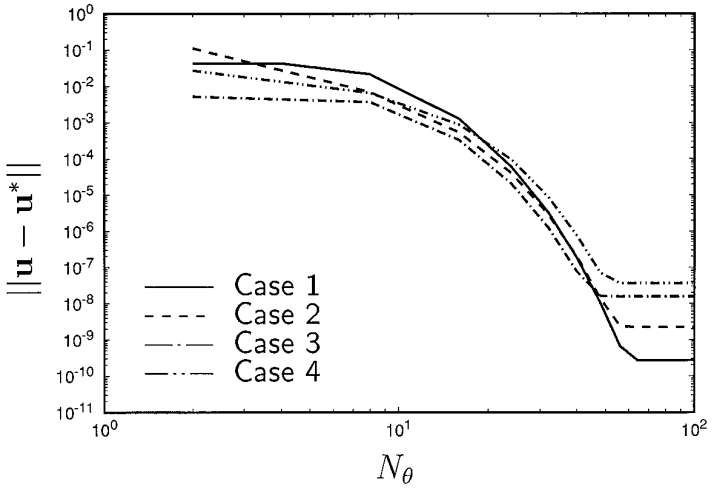


**FIG. 9.** Effect of increasing the number of azimuthal modes in the matching procedure on the norm of the velocity error for all four test cases.

## 5. NONZERO VORTICITY ON MATCHING BOUNDARY

The development of this method so far has been simplified by the assumption that the condition of zero vorticity on the computational boundary has been met. In practice this will rarely be true. Thus, as a practical consideration, it is useful to know the relationship between the level of vorticity on the matching boundary and the associated error in the velocity.

Vorticity on the matching boundary produces rotational flow of equivalent magni-

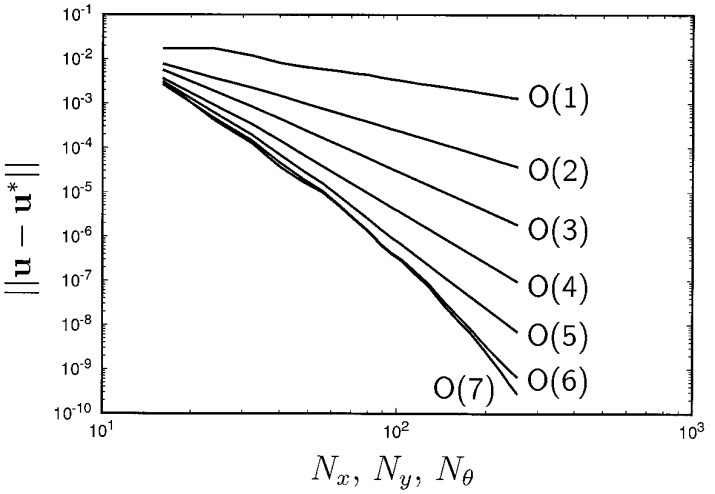


**FIG. 10.** Norm of the velocity error vs mesh resolution for Case 1. Curves are labeled with the order of accuracy for the interpolation scheme used.

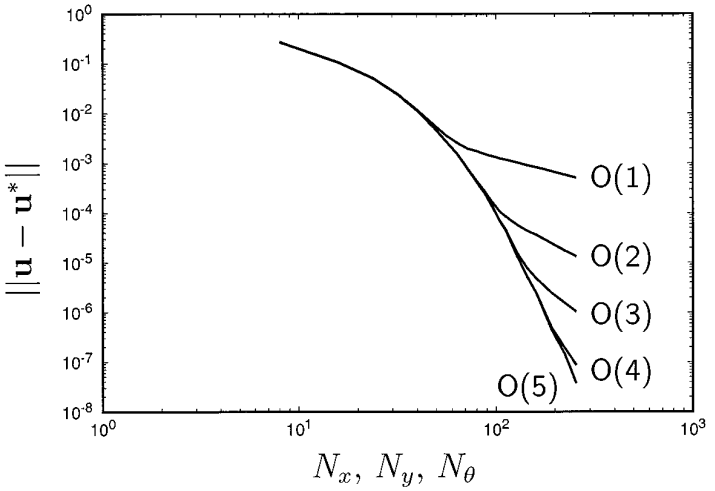


**FIG. 11.** Norm of the velocity error vs mesh resolution for Case 4. Curves are labeled with the order of accuracy for the interpolation scheme used.

tude on the boundary. These rotational velocities can be considered an error which is added to the irrotational velocities used in the computation of the matching coefficients in (21). Constructing the potential velocities from these coefficients produces an error that is linearly proportional to the level of vorticity on the matching boundary. Although not obvious from the form of (21), the magnitude of these velocity errors is, at most, equal to the magnitude of vorticity on the matching boundary.

Spurious vorticity in the external domain (that is, in the external part of the computational domain, but not on the matching boundary) produces irrotational velocity on the matching boundary. This irrotational velocity is, to the method, indistinguishable from the irrotational velocity due to the image vorticity in (4), in the sense that it does not match the known form, (9) and (10), for a domain which is unbounded in two directions. Thus, the matching procedure removes this spurious velocity. If vorticity exists in the external domain because the true vorticity field never decays to zero or it has been diffused by viscosity, then, provided this external vorticity decays at least exponentially fast (as viscous diffusion will provide), a Green's function analysis of (4) shows that the magnitude of the velocity due to the unrepresented vorticity is, at most, of equal magnitude and linearly proportional to the level of vorticity on the matching boundary.

The end result is that the global velocity error is linearly proportional to the level of vorticity on the matching boundary. This result was tested by adding spurious vorticity, with its peak on the matching boundary, to each of the test cases. With everything else held constant, the global error in velocity was shown to vary exactly linearly with the amplitude of the spurious vorticity.

For comparison, a two dimensional version of the test done by Corral and Jiménez [8, Fig. 2b] is performed using a Gaussian vorticity distribution of

$$\omega_z = e^{-r^2} \tag{28}$$

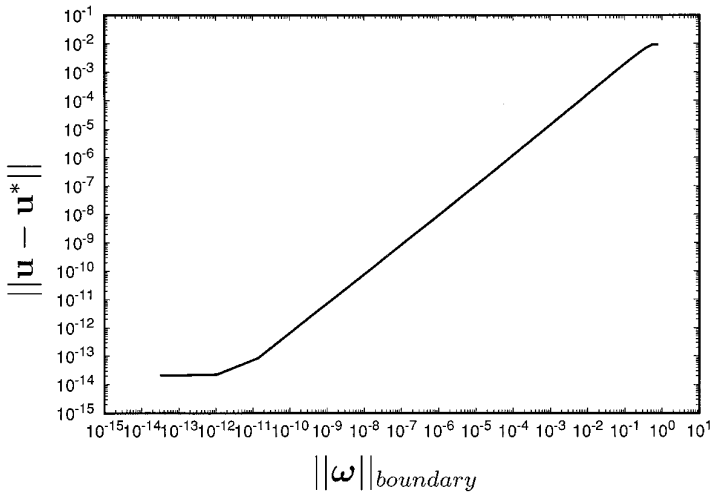


**FIG. 12.** Global error in velocity vs vorticity on the matching boundary for a columnar Gaussian vortex.

and a corresponding reference velocity distribution of

$$\mathbf{u}^* = \frac{1}{2r}(1 - e^{-r^2})\mathbf{e}_\theta. \tag{29}$$

The velocity computation is performed on a number of domains of different sizes such that the magnitude of vorticity on the boundary varies significantly. The cross-axial domain sizes are varied from 1 to 13. The mesh density is kept constant at 24 meshpoints per unit length. The global error in velocity versus the level of vorticity on the matching boundary is presented in Fig. 12. The norm of the vorticity on the matching boundary is computed as

$$\|\boldsymbol{\omega}\|_{boundary} = \left[\frac{1}{A}\int_A |\boldsymbol{\omega}|^2 \, dA\right]^{1/2}, \tag{30}$$

where $A$ is the matching boundary. The velocity error is linear with respect to the vorticity on the matching boundary.

Another practical test is to compute the global error in velocity for vorticity distributions which are placed so that finite vorticity exists on the matching boundary. This was done for each of the four test cases described in Section 4.1. The results, presented in Fig. 13, show that global error in the velocity is approximately linearly proportional to $\|\boldsymbol{\omega}\|_{boundary}$ and that for all cases the magnitude of the global error in velocity is less than the magnitude of vorticity on the matching boundary.

The end result is equivalent to the conclusion arrived at by Corral and Jiménez. So long as the magnitude of the vorticity on the matching boundary does not exceed

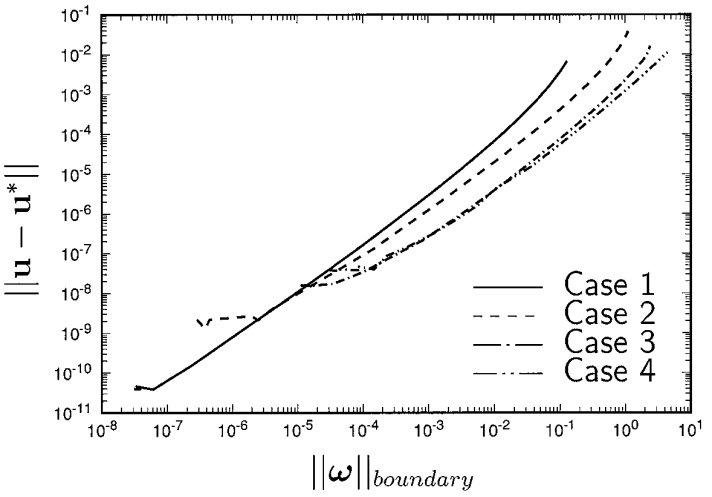


**FIG. 13.** Global error in velocity vs vorticity on the matching boundary for the four test cases.

the magnitude of the vorticity resolution error elsewhere in the internal domain, the magnitude of the global velocity error will not be affected.

## 6. NONZERO VORTICITY ON COMPUTATIONAL BOUNDARY

Because the velocity field is, in general, nonperiodic, when finite amounts of vorticity reach the computational boundary (recall that this is the surface of the cubic region in Fig. 1), the nonlinear term in the vorticity transport equation will also be nonperiodic. When this nonlinear term is formed as written in (1), $-\nabla \times (\boldsymbol{\omega} \times \mathbf{u})$, this non–periodicity results in Gibbs phenomenon errors. As Corral and Jiménez note, for 2D flows this nonlinear term reduces to just the convection term. When computed in this manner, $-(\mathbf{u} \cdot \nabla)\ \boldsymbol{\omega}$, no derivatives of the discontinuous velocity field are taken and the Gibbs errors, while still present, are substantially reduced. In 3D flows this advantage is lost due to the vortex stretching term.

In the present case we are primarily interested in 3D flows and we wish to form the nonlinear term as written in (1) since it is computationally more efficient. Figure 14 shows a pair of counterrotating vortices convecting themselves through the lower computational boundary. Gibbs phenomenon errors are clearly present. However, under normal circumstances these Gibbs phenomenon errors can be shown to have a magnitude which is equal to or less than the magnitude of the vorticity on the computational boundary and the previous conclusion remains essentially unchanged. As long as the level of vorticity on the computational boundary is of equal or lesser magnitude than the vorticity errors elsewhere in the domain, the magnitude of the error in the time derivative of vorticity will not be affected.

To show this, let us assume that a vortex of circulation $\Gamma$ has approached to within a distance $L$ of the computational boundary (see Fig. 15). Let $N$ represent the number of mesh points spanned by $L$. We can estimate the magnitude of the

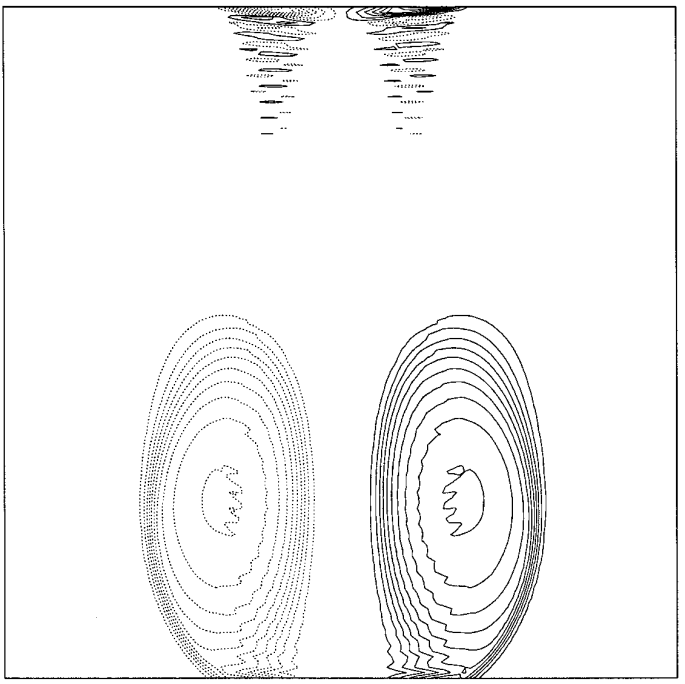

**FIG. 14.** Vorticity field as a pair of counterrotating vortices convect themselves through the computational boundary. Solid contours represent positive vorticity. Dotted contours represent negative vorticity. The square box is the computational boundary.

velocity on the computational boundary as $\Gamma/2\pi L$. Assuming a finite level of vorticity on the computational boundary with magnitude $\omega_b$, the cross product of vorticity and velocity has a magnitude $|\boldsymbol{\omega} \times \mathbf{u}| \approx \Gamma\omega_b/2\pi L$. A conservative (large) estimate of the magnitude of the curl of this quantity is found dividing it by one half the mesh spacing, or $|\nabla \times (\boldsymbol{\omega} \times \mathbf{u})| \approx \Gamma\omega_b N/\pi L^2$. We shall estimate the discontinuity of this quantity on the computational boundary by multiplying by two. The maximum amplitude of the Gibbs phenomenon is about 10% of the amplitude of the discontinuity [6]. Thus, the magnitude of the Gibbs phenomenon errors in the time derivative of vorticity is $|\partial\boldsymbol{\omega}/\partial t| \approx 0.2\Gamma\omega_b N/\pi L^2$. Based on a convective CFL number of one,

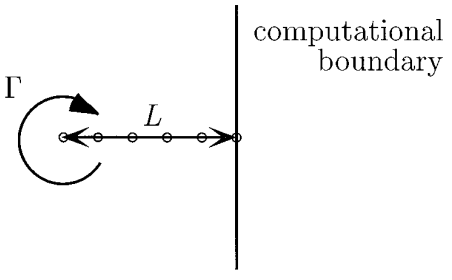


**FIG. 15.** Diagram showing the symbols used in Section 6.

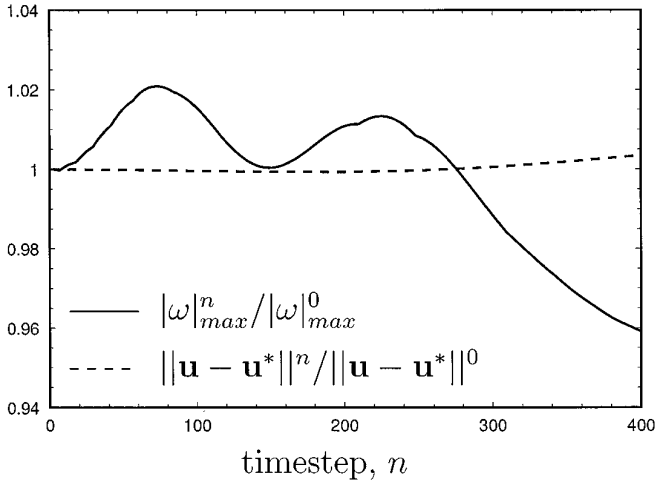


**FIG. 16.** Magnitude of the maximum vorticity on the computational boundary and the global error in velocity, normalized by their initial values, over 400 RK4 timesteps for an isolated Gaussian vortex.

each timestep is $2\pi L^2/\Gamma N$. Thus, at every timestep, the magnitude of the Gibbs error in the vorticity update is not more than $0.4\omega_b$, and does not change the magnitude of the error already present.

This simple analysis does not address the compounding effect of time, the diminishing effect of viscosity, the smoothing effect of de-aliasing or the cancelation which would occur over many timesteps when the vorticity errors near the computational boundary oscillate about zero. A computational test of this effect was performed by initializing the vorticity field with the a Gaussian distribution of vorticity, as defined by (28), over a $6 \times 6 \times 1$ domain using a $128 \times 128 \times 4$ mesh. The maximum vorticity on the computational boundary for this case should be $2.3 \times 10^{-16}$. Applying the $\frac{2}{3}$ rule to the initial vorticity field (truncating of the Fourier series) places vorticity on the computational boundary with a maximum value of $1.3 \times 10^{-4}$. Thus, since a relatively large amount of vorticity exists on the computational boundary and the velocity field is nonperiodic, we would expect this to be a clean test of the Gibbs errors in the nonlinear term. This field was advanced in time for 400 RK4 timesteps using a CFL number of 1 at $\mathrm{Re} = \infty$. Figure 16 shows the development of the maximum level of vorticity on the computational boundary and the global error in velocity, normalized by their initial values. The slight variation in velocity error, and the eventual decrease of the maximum vorticity magnitude on the boundary, indicates that the Gibbs phenomenon errors in the nonlinear term are not causing problems.

In this section we have shown that large scale vorticity on the computational boundary can be catastrophic due to Gibbs phenomenon errors. We have also shown that for low levels of vorticity on the computational boundary these Gibbs errors are bounded at an equivalent magnitude and that in practice they are benign. We will conclude by saying, in our experience, when the magnitude of vorticity on the computational boundary is kept low, Gibbs phenomenon errors in the nonlinear terms do not upset the accuracy of the computation.

**TABLE I**
**Table Showing the Relative Increase in CPU Cost for the Method Presented Here vs Periodic Extension in All Directions or the Method of Corral and Jiménez**

| $N_x$ and $N_y$ | $N_\theta$ | Interpolation order | % increase in cpu cost for velocity computation | % increase in cpu cost for time advancement |
|---|---|---|---|---|
| 256 | 512 | 6 | 115 | 40 |
| 256 | 512 | 3 | 55 | 20 |
| 128 | 256 | 6 | 125 | 45 |
| 128 | 256 | 3 | 65 | 20 |

## 7. EFFICIENCY

Unlike the method due to Corral and Jiménez, the cost for implementing this analytical matching condition is not negligible. Depending on the mesh size and the order selected for the interpolation routine, the cost to compute the potential flow correction can be more than the cost of the vorticity–velocity computation (4). Even when the cost of an entire time advancement step is considered, this method can take 50% more time than a method using periodically extended boundaries in all directions. Table I shows the relative increase in cpu times for this method versus using periodically extended boundaries for several different mesh sizes and interpolation orders. Since the 1D analytical matching of Corral and Jiménez incurs almost no more cost than the periodically extended boundary case, these numbers represent the increase in time over that method as well. These numbers were taken from our implementation of the present method on a Cray C90 making extensive use of the solid-state storage devices to reduce core memory size. They are based on a velocity computation and a first-order Euler time advancement step by themselves. No initialization, output or postprocessing is included. The mesh sizes quoted represent the mesh sizes used before de-aliasing. The results clearly show high cost of the Lagrange interpolation. Cpu times for other implementations on other systems may vary significantly, but should not affect the conclusions.

Much more important than the cpu time required for a given mesh is the cpu time required to achieve a suitably accurate result. This is the most practical measure of the value of a method. To assess this, the relationship between error in the result and the cpu time used is found for the three applicable boundary treatments; 3D periodic extension, Corral and Jiménez's method, and the present method. These trends are computed using a vorticity field which contains two counterrotating columnar vortices with mean vorticity given by (25). The vortices have unit radius and a core separation of two. Vorticity contours for this case are shown in Fig. 17. Velocity contours are shown in Fig. 18. In these figures the square computational domain and circular matching boundary (for the present method) are also shown. This emphasizes the level of velocity in the external domain and the proximity to which significant vorticity approaches the matching boundary. In every case, all parameters were adjusted to achieve the minimum error for a given amount cpu time. For the 3D periodic extension, this involved adjusting the cross-axial extent

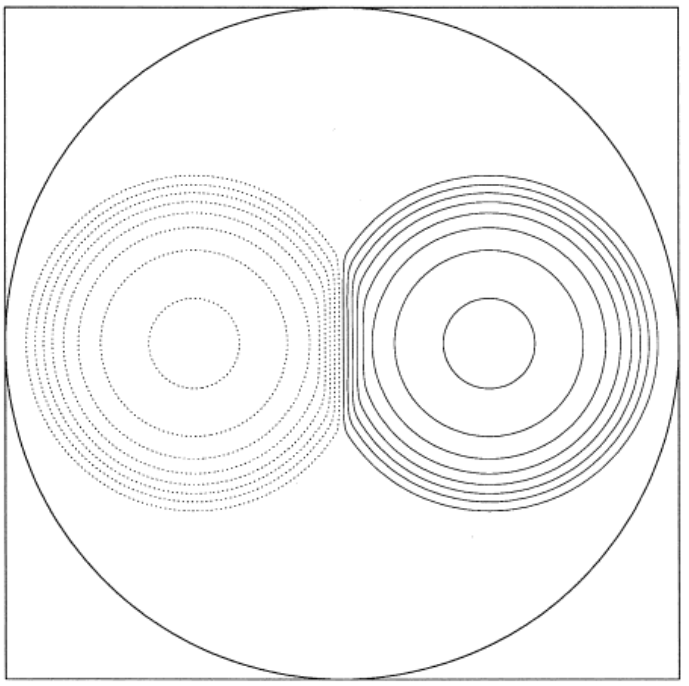

**FIG. 17.** Vorticity contours of the test case used in Section 7. Negative vorticity is shown by a dotted line. Contour magnitudes begin at $\pm 0.025$ and step by 0.05. The square box denotes the limits of the computational domain and the circle represents the matching boundary.

of the domain for every mesh. For the Corral and Jiménez method, this involved adjusting the extent of the domain in the periodic cross-axial direction and the mesh density in the analytically extended cross-axial direction. Figure 19 shows the error in velocity versus the cpu time required for the velocity computation for the three relevant boundary treatments. When compared in this manner, the current scheme shows a remarkable improvement over other methods. While it is more expensive for a given mesh size, it can be orders of magnitude less expensive for a given accuracy.

## 8. SAMPLE PROBLEMS

This section shows two applications of the boundary treatment developed in this paper. In both cases, the flow is representative of an aircraft's vortex wake, the problem which motivated the development of this method.

### 8.1. *Crow Instability*

The first example is the 3D simulation of a pair of perturbed, incompressible, counterrotating columnar vortices. The goals of this simulation are to reproduce the Crow instability [17] in a three-dimensional nonlinear calculation for a configuration that is representative of actual aircraft vortices and to track the growth of

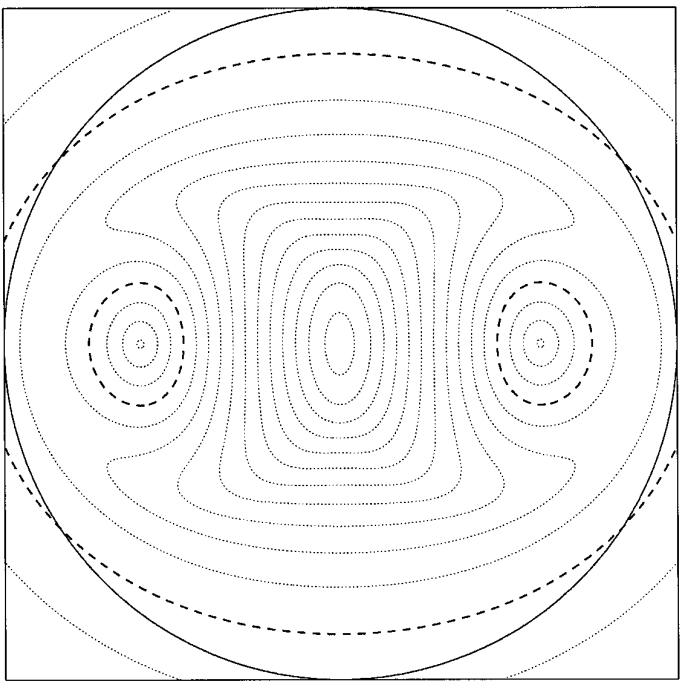

**FIG. 18.** Velocity magnitude contours of the test case used in Section 7. Contour magnitudes begin at $\pm 0.005$ and step by 0.02. The dashed contour represents a velocity magnitude of 0.065 (22% of peak). The square box denotes the limits of the computational domain and the circle represents the matching boundary.

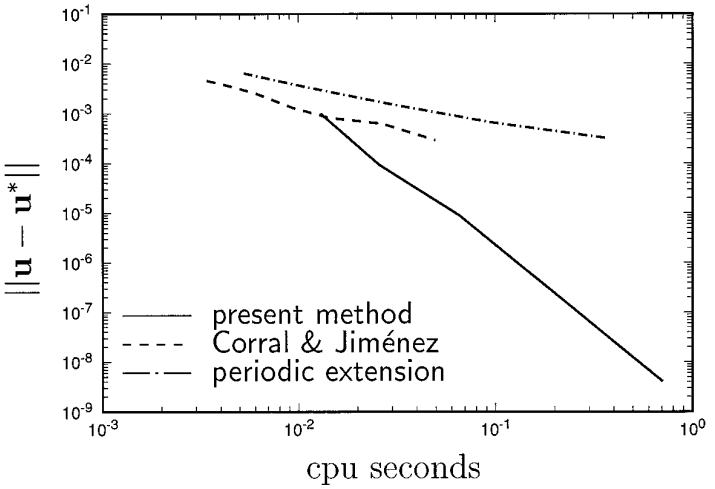


**FIG. 19.** Global error in velocity vs cpu time required by the velocity computation is shown for (1) domains which are analytically extended in two directions, (2) domains which are analytically extended in one direction and periodic in the other two, and (3) domains which are periodically extended in all directions.

the instability through the linear and nonlinear regimes. See Rennich and Lele [18] for details.

To make this simulation representative of aircraft vortices, the estimated vortex core diameter to wingspan ratio due to Spreiter and Sacks [19] is used, resulting in a vortex separation of 10.190. All quantities continue to be nondimensionalized following the definitions in Section 4.1, with the addition of a second dimensionless time scale, $\Gamma_0/2\pi b^2$, where $b$ is the separation of the two vortices (span). This second dimensionless time is often used when studying the Crow instability and is given in parenthesis following the first.

Following Crow's analysis, the most unstable axial wavenumber for such a configuration is $k = 0.07221$. Since Crow's analysis assumes a Rankine vortex profile, the configuration requires an adjustment to account for the smooth vortices used here. This is done by modifying the perturbation wavenumber so that the perturbation eigenvalue, $\sigma$, for bending waves on the smooth vortices, matches the eigenvalue for the Rankine vortices perturbed at the original wavenumber. That is, the perturbation wavenumber is adjusted so that the self-induction velocities are equal. Since we are interested in the linear growth of the Crow instability, the vortices are perturbed with symmetric sinusoidal perturbations inclined at 45° to the plane containing both vortices. This shape very closely approximates the Crow eigenmode. The initial amplitude of each perturbation is 0.015. The Reynolds number based on circulation for this case, $\mathrm{Re} = \Gamma/\nu$, is 100,000.

The computation was performed in several stages. The simulation was initiated on a $20 \times 20 \times 85.268$ domain with a $128 \times 128 \times 4$ mesh. This domain was large enough to allow significant growth of the instability and contained only enough points in the axial direction to resolve the mean and fundamental modes. This axial resolution was presumed sufficient during the linear growth of the instability and would conserve cpu time. At $t = 1633.68$ (2.50403), the solution was interpolated to a mesh with 128 points in the axial direction so that any nonlinear interactions would be resolved. Finally, towards the end of the simulation, the solution was interpolated to a $30 \times 30 \times 85.268$ domain with a $192 \times 192 \times 128$ mesh to accommodate further growth of the instability.

Figure 20 shows three snapshots of vorticity. These clearly show how a pair of counterrotating vortices, with an imperceptible initial perturbation, evolves into the Crow instability. Figure 21 shows a perspective view of the vorticity contours at the late time.

The growth of the instability can be tracked by computing the maximum cross-axial displacement in the centroid of axial vorticity of each vortex. This is essentially the quantity used by Crow in his analysis. Figure 22 compares the computed growth of the instability with the growth predicted by Crow's linear, inviscid, vortex filament analysis. The two curves are indistinguishable for well over a decade of growth. Towards the end of the simulation nonlinear effects become important and cause the computed growth rate to accelerate.

This simulation shows the size of the instability beyond which nonlinear effects become important. The close match between the observed and predicted amplification rate demonstrates the validity of Crow's linear, inviscid analysis. Further studies of the Crow instability performed using this method are described in [20].

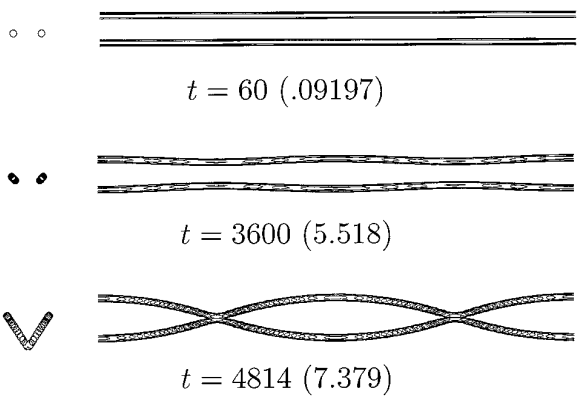


**FIG. 20.** Vorticity contours, $|\omega| = 0.05$, for the Crow instability simulation. End and top views are shown.

### 8.2. *2D Wake from an Idealized Flapped Wing*

As a second example we compute the evolution of the 2D wake due to an idealized flapped wing. Here we are interested in gaining a qualitative understanding of the flow. The flapped wing is idealized as a summation of two elliptical lift distributions, with equal root circulation and spans which are different by a factor of two. Total root circulation $\Gamma_0$ is set to one. The effective span of the wake, defined as

$$b_0 = \frac{1}{\Gamma_0} \int_{-b/2}^{b/2} \Gamma(x)\, dx \tag{31}$$

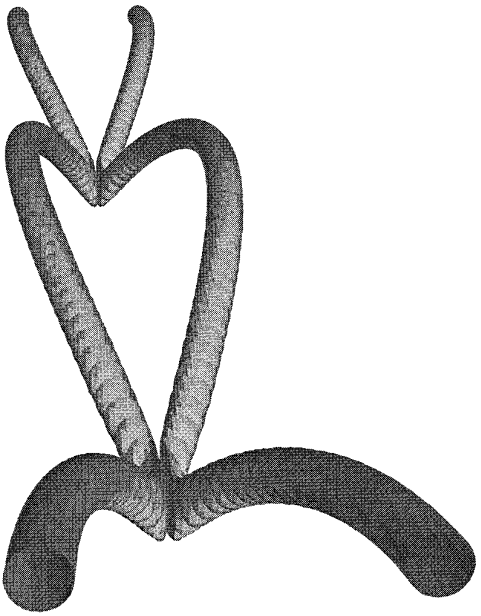

**FIG. 21.** Perspective view of the fully developed Crow instability. Isosurface of vorticity at $|\omega| = 0.05$ is shown; $t = 4814$ (7.379).

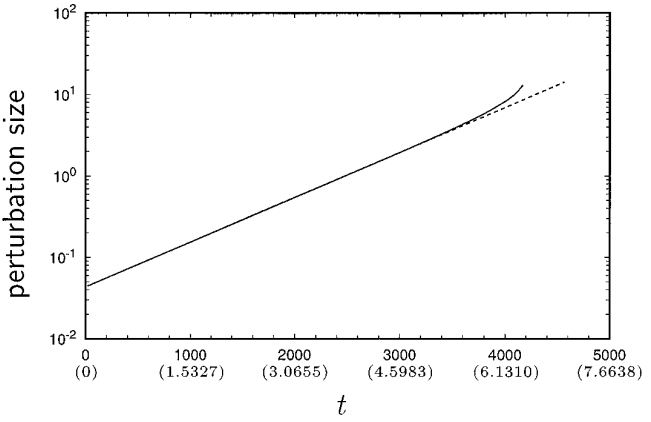


**FIG. 22.** Growth of the Crow instability. The solid line shows the computed result and the dashed line shows the prediction of Crow's linear, inviscid analysis.

is set equal to the span of the vortex pair in the previous case, $b_0 = 10.190$. The resulting circulation distribution is given in Fig. 23. Following the work of Spalart [21], this one-dimensional circulation distribution is convolved with a Gaussian smoothing function,

$$\frac{1}{\pi\varepsilon^2}\exp\left(-\frac{x^2+y^2}{\varepsilon^2}\right), \tag{32}$$

to produce a smooth, two-dimensional vorticity distribution. We used $\varepsilon = 0.2$. Since there is no longer an initial columnar vortex, the length scale by which the problem is nondimensionalized needs to be clarified. We now use Spreiter and Sacks' estimate of the core size, $0.0981b_0$ [19]. The result is that the time scales for the two sample problems are equivalent. The Reynolds number based on circulation for this calculation is $\Gamma/\nu = 10{,}000$. A mean vertical velocity of $\Gamma_0/2\pi b_0$ is prescribed so that the vorticity remains centered in the computational domain.

Figure 24 shows six snaphots of vorticity for the evolving flapped wake. The initially planar sheet of vorticity rolls up into four nearly circular vortices. As the tip vortices get convected through the flap vortices, they can be seen to deform slightly.

Figure 25 shows the last three snapshots of Fig. 24 with contours in log scale.

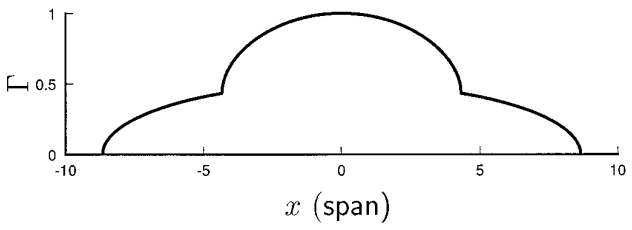


**FIG. 23.** Bound circulation distribution for an idealized flapped wing.

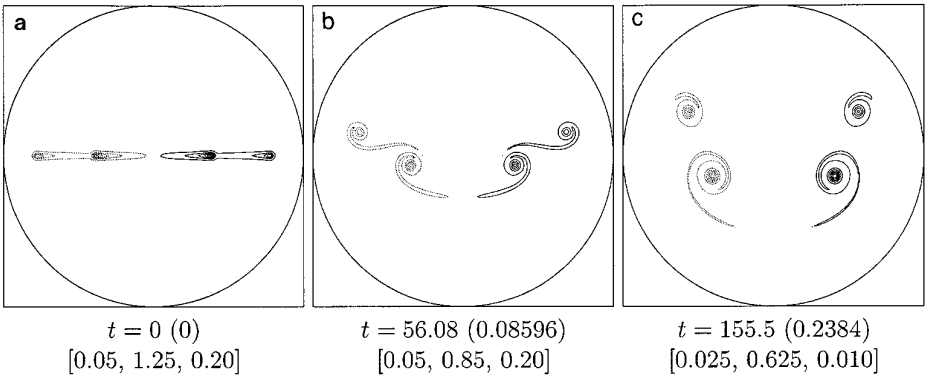


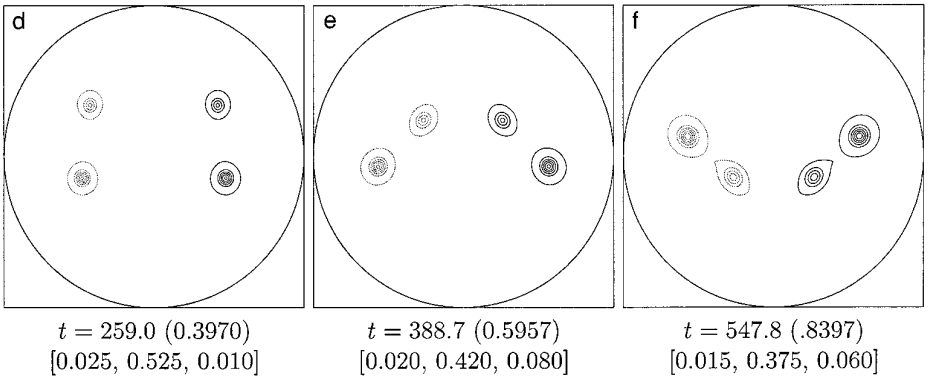


**FIG. 24.** Vorticity contours of an evolving 2D flapped wake. Solid contours represent positive vorticity. Dotted contours represent negative vorticity. The magnitudes of the contours are given below each figure as [*initial, final, interval*]. The square box represents the limits of the computational domain. The circle represents the matching boundary.

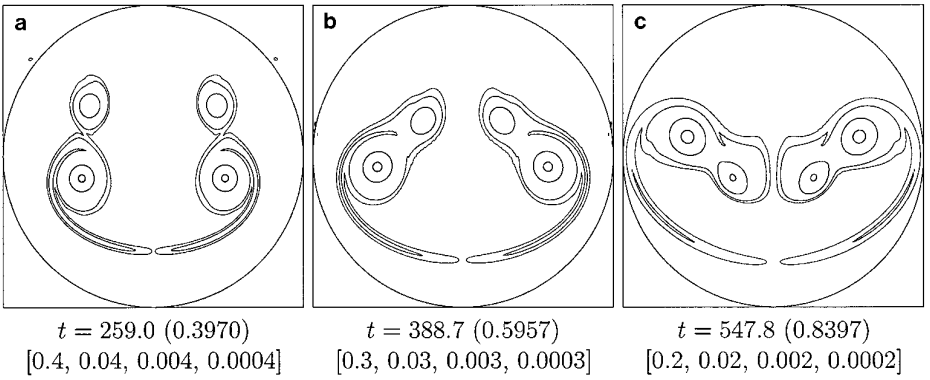


**FIG. 25.** Contours of vorticity magnitude for an evolving 2D flapped wake. The contours are in log scale with the individual levels given below each figure in brackets. The square box represents the limits of the computational domain. The circle represents the matching boundary.

This scaling shows regions of low vorticity in much greater detail. These plots emphasize the high resolution of the calculation and the extent to which significant vorticity fills the domain. Most importantly these plots demonstrate how closely vorticity can approach the matching boundary without causing any appreciable error. The first two snapshots in Fig. 25 have contours adjusted so that a small amount of spurious vorticity can be seen near the matching boundary. In the third snapshot this spurious vorticity has disappeared, further demonstrating that small levels of vorticity on or outside of the matching boundary do not pose a hazard.

## 9. CONCLUSIONS

We have successfully extended the analytical matching boundary condition due to Corral and Jiménez [8] to flows which are unbounded in two directions. The method has been fully described and its accuracy verified. When compared to other methods applicable to incompressible vortical flows in 2D unbounded domains, this method has been shown to be advantageous. When accurate results are required, this method can be orders of magnitude more efficient than others currently in use. Finally we have presented the results of two sample calculations which demonstrate that the method is useful for problems of current interest.

## ACKNOWLEDGMENTS

This work was supported by the National Science Foundation and the Boeing Commerical Airplane Company under the PYI award to SKL. We would also like to acknowledge the Numerical Aerodynamic Simulation Facility and the San Diego Supercomputing Center for providing computational resources.

## REFERENCES

1. C. E. Grosch and S. A. Orszag, Numerical solution of problems in unbounded regions; Coordinate transforms, *J. Comput. Phys.* **25,** 273 (1977).
2. J. P. Boyd, The optimization of convergence for Chebyshev polynomial methods in an unbounded domain, *J. Comput. Phys.* **45,** 43 (1982).
3. S. A. Orszag and A. T. Patera, Secondary instability of wall-bounded shear flows, *J. Fluid. Mech.* **128,** 347 (1983).
4. A. B. Cain, J. H. Ferziger, and W. C. Reynolds, Discrete orthogonal function expansions for non-uniform grids using the fast Fourier transform, *J. Comput. Phys.* **56**(2), 272 (1984).
5. R. W. Metcalfe, S. A. Orszag, M. E. Brachet, S. Menon, and J. J. Riley, Secondary instability of a temporally growing mixing layer, *J. Fluid. Mech.* **184,** 207 (1987).
6. C. Canuto, M. Y. Hussaini, A. Quarteroni, and T. A. Zang, *Spectral Methods in Fluid Dynamics* (Springer-Verlag, Berlin/Heidelberg/New York, 1988).
7. P. R. Spalart, R. D. Moser, and M. M. Rogers, Spectral methods for the Navier–Stokes equations with one infinite and two periodic directions, *J. Comput. Phys.* **96,** 297 (1991).
8. R. Corral and J. Jiménez, Fourier/Chebyshev methods for the incompressible Navier–Stokes equations in infinite domains, *J. Comput. Phys.* **121,** 261 (1995).
9. P. R. Spalart, *Numerical Simulation of Boundary Layers: Part 1. Weak Formulation and Numerical Method.* NASA TM 88222, Ames Research Center, February 1986.
10. R. Sondergaard, *Direct Numerical Simulation of a Temporally Evolving Incompressible Plane Wake:*

*Effect of Initial Conditions on Evolution and Topology,* Technical Report SUDAAR-667, Stanford University Department of Aeronautics and Astronautics, 1995.

11. C. R. Anderson and M. B. Reider, A high order explicit method for the computation of flow about a circular cylinder, *J. Comput. Phys.* **125,** 207 (1996).
12. M. Abramowitz and I. A. Stegun (Eds)., *Handbook of Mathematical Functions* (Dover, New York, 1972), p. 376.
13. L. N. Howard and A. S. Gupta, On the hydrodynamic and hydromagnetic stability of swirling flows, *J. Fluid. Mech.* **14,** 463 (1962).
14. S. E. Widnall, D. Bliss, and A. Zalay, Theoretical and experimental study of the stability of a vortex pair, in *Aircraft Wake Turbulence and Its Detection* (Plenum, New York, 1971), p. 305.
15. D. W. Moore and P. G. Saffman, The motion of a vortex filament with axial flow, *Phil. Trans. R. Soc. Lond.* **272,** 403 (1972).
16. M. V. Melander and F. Hussain, Topological vortex dynamics in axisymmetric viscous flows, *J. Fluid. Mech.* **260,** 57 (1994).
17. S. C. Crow, Stability theory for a pair of trailing vortices, *AIAA J.* **8**(12), 2172 (1970).
18. S. C. Rennich and S. K. Lele, Direct numerical simulation of the breakdown of aircraft wake vortices, in *The Characterisation & Modification of Wakes from Lifting Vehicles in Fluids,* AGARD-CP-584, 1996.
19. J. R. Spreiter and A. H. Sacks, The rolling up of the trailing vortex sheet and its effect on the downwash behind wings, *J. Aeronaut. Sci.* **18**(1), 21 (1951).
20. S. C. Rennich, *Accelerated Destruction of Aircraft Wake Vortices,* Ph.D. thesis, Stanford University Department of Aeronautics and Astronautics, 1997.
21. P. R. Spalart, On the motion of laminar wing wakes in a stratified fluid, *J. Fluid. Mech.* **327,** 139 (1996).